Research Article Vol. 2, No. 5 / 15 May 2019 / OSA Continuum 1539

Modeling axial irradiance distortion in holographic optical needles produced with high numerical aperture lenses

DAVID MALUENDA,[1] IGNASI JUVELLS,[2] ROSARIO MARTÍNEZ-HERRERO,[3] AND ARTUR CARNICER[2,*]

[1] *Centro Nacional de Biotecnología (CSIC), Darwin, 3, Campus Universidad Autonoma de Madrid, 28049 Cantoblanco, Madrid, Spain*
[2] *Universitat de Barcelona (UB), Facultat de Física, Departament de Física Aplicada, Martí i Franquès 1, 08028 Barcelona, Spain*
[3] *Departamento de Óptica, Facultad de Ciencias Físicas, Universidad Complutense de Madrid, Ciudad Universitaria, 28040 Madrid, Spain*
[*] *artur.carnicer@ub.edu*

Abstract: Optical needles produced by means of diffractive technology might display limited quality and uniformity. It has been suggested that the bulky optical elements present on these setups can be responsible of such behavior. In particular, issues such as the lack of flatness of the optical components, modulation errors in the holographic displays, and optical aberrations might degrade the quality of the needle. In this paper, we model how these variables affect the uniformity of the irradiance of the needle on the propagation axis. A comparison between experimental and computationally estimated results is provided.

1. Introduction

Recently, a large number of papers dealing with the design of long optical needles using high numerical aperture (NA) systems have been published [1–17]. This topic has attracted the attention of many groups because of potential applications in imaging, lithography or particle acceleration among others [18–20]. In a previous paper [21], we designed highly focused polarized holographic optical needles (HON) with almost constant irradiance on the optical axis. Despite the overall quality of produced beams was very high, the needles presented a noticeable non-uniform appearance in several places. Interestingly, similar issues were reported by other authors as well [10,22]. In particular, it has been suggested that misalignment, lack of flatness of the optical components, modulation errors in the holographic displays, and optical aberrations might degrade the quality of the needle. The present paper aims to analyze how these issues affect the behavior of HON produced with high NA lenses. In order to provide a better understanding on how an experimental needle differs from the ideal case, we developed a comprehensive numerical simulation that takes into account the effects of the different sources of degradation.

The paper is organized as follows: in section 2 we review key concepts on the production HON. In sections 3, we present experimental results and the corresponding analysis. Finally, the conclusions are presented in section 4. The developed software is available on-line as a supplementary material [23].

2. Production of holographic optical needles

The Richards-Wolf equation [24] describes the behavior of the electric field $\mathbf{E}$ near the focal plane of an aplanatic high NA microscope lens. Let $\mathbf{E_0}$ be vector angular spectrum of the illuminating

#358441 https://doi.org/10.1364/OSAC.2.001539
Journal © 2019 Received 23 Jan 2019; revised 12 Mar 2019; accepted 18 Mar 2019; published 1 Apr 2019

OSA CONTINUUM

field field $\mathbf{E_s}$, namely

$$\mathbf{E}_0 = \sqrt{\cos\theta}\,((\mathbf{E}_s \cdot \mathbf{e}_1)\,\mathbf{e}_1 + (\mathbf{E}_s \cdot \mathbf{e'}_2)\,\mathbf{e}_2)\,. \tag{1}$$

$\mathbf{e}_1$ and $\mathbf{e}_2$ are unit vectors on the azimuthal and radial directions at the sphere of reference and θ and φ are the polar and the azimuthal angles respectively; $\mathbf{e'}_2$ is the projection of $\mathbf{e}_2$ on the entrance pupil:

$$\mathbf{e}_1 = (-\sin\varphi, \cos\varphi, 0) \tag{2a}$$

$$\mathbf{e}_2 = (\cos\theta\cos\varphi\,,\ \cos\theta\sin\varphi\,,\ \sin\theta\,) \tag{2b}$$

$$\mathbf{e'}_2 = (\cos\varphi\,,\ \sin\varphi\,,\ 0)\,. \tag{2c}$$

The Richards-Wolf equation reads

$$\mathbf{E}(r,\phi,z) \propto \int_0^{\theta_0}\int_0^{2\pi} \mathbf{E}_0(\theta,\varphi) e^{ikr\sin\theta\cos(\phi-\varphi)} e^{-ikz\cos\theta}\sin\theta\,\mathrm{d}\theta\,\mathrm{d}\varphi \tag{3}$$

where $k = 2\pi/\lambda$ is the wave number and (r,ϕ,z) are the coordinates at the focal area. The numerical aperture (NA) is related to the maximum θ angle: NA=$\sin\theta_0$. Figure 1 summarizes the vectors and geometrical variables involved in the problem. Note that $\mathbf{e}_x$, $\mathbf{e}_y$ and $\mathbf{e}_z$ are unit orthogonal vectors in the directions of the coordinate axes.

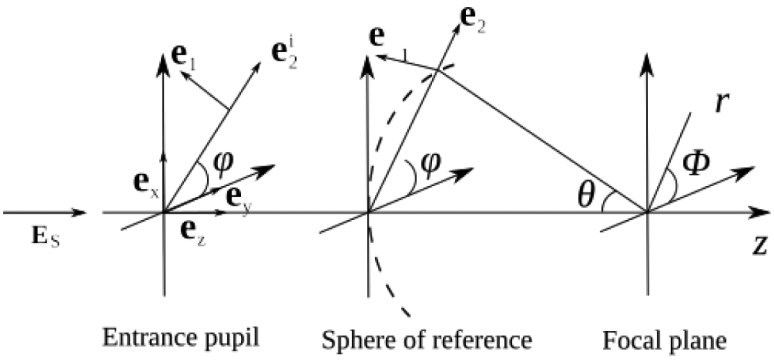

Fig. 1. Coordinate systems and geometrical variables.

Figure 2 shows the sketch of an optical system able to produce HON. The system is illuminated by means of a He-Ne laser with $\lambda = 594$ nm. The beam passes through a linear polarizer (LP) and a spatial light modulator (SLM) used for displaying a modulation function $h(\theta)$ as a computer generated hologram. This distribution modifies the wave-front so that the focused field verifies certain required properties. In the present experiment, we use a Holoeye HEO-0017 translucent display. The half-wave and the quarter-wave plates, and the polarizers are required to set up the SLM. Relay lenses L_1 and L_2 image the input beam $\mathbf{E}_s$ on the entrance pupil of the microscope lens (ML). The spatial filter (SF) is required to remove high order holographic terms. Since the beam is split using beam splitter BS, the irradiance $|\mathbf{E}_s|^2$ can be recorded on CCD1 for inspection purposes. The irradiance of the focused field $I(r,z) = |\mathbf{E}(r,z)|^2$ is detected at the observation plane (a microscope slide) and subsequently recorded by camera CCD2 with the help of the tube lens (TL). The position of the slide is tuned by means of a piezoelectric actuator (Newport LTA-HL) with a minimum incremental motion of 50 nm. Note that since the NA of the TL is very low, the longitudinal component of $\mathbf{E}$ cannot be recorded [25,26].

In what follows and without loss of generality, the illumination beam displays a Gaussian profile and $\mathbf{E}_S$ is assumed to be linearly polarized in the x-direction. Then, the field $\mathbf{E}_s$ at the

OSA CONTINUUM

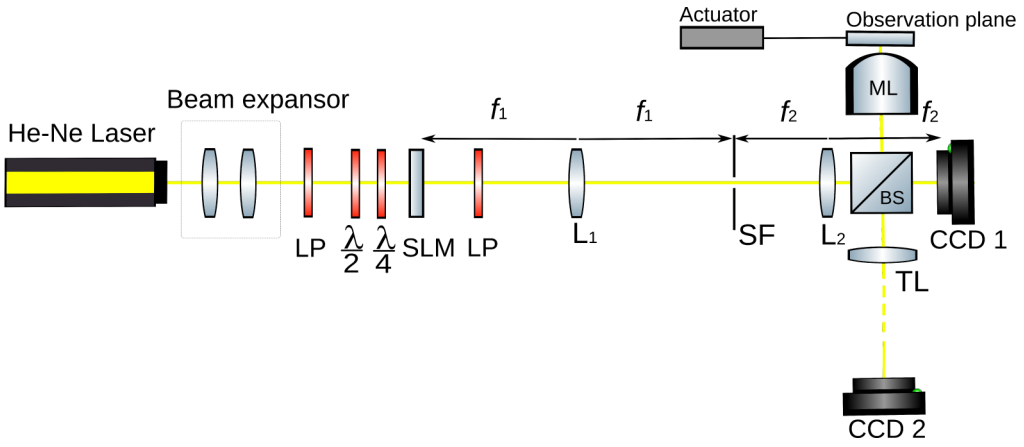

Fig. 2. Optical setup: LP: linear polarizer, $\lambda/2$: half-wave plate, $\lambda/4$: quarter-wave plate, SLM: spatial light modulator, L_1 (f_1= 100 mm) and L_2 (f_2 = 50 mm), SF: spatial filter, TL: tube lens (f_{TL}= 400), ML: microscope lens (NA=0.65), CCD1 and CCD2: cameras.

sphere of reference is described by

$$\mathbf{E}_s(\theta,\varphi) = \exp\left(-\frac{\sin^2\theta}{f_0^2\sin^2\theta_0}\right) h(\theta)\,\mathbf{e}_x, \tag{4}$$

where f_0 is the filling factor. In order to produce a long focused field, the following modulation function $h(\theta)$ was recently proposed [21]

$$h(\theta) = N\,\mathrm{sinc}\left(2\pi N\frac{\cos\theta-(1+\cos\theta_0)/2}{1-\cos\theta_0}\right)\sin\theta; \tag{5}$$

here, $\mathrm{sinc}(x) = \sin(x)/x$ is the unnormalized cardinal sine function. A similar mask, intended for paraxial scalar axicons, was described in [27]. Note that $h(\theta)$ displays interesting mathematical properties: (i) the length of the needle is determined by N, (ii) $h(0) = 0$, (iii) no jump discontinuity at the edge of the entrance pupil of the microscope lens exists (i.e. $h(\theta_0) = 0$) and (iv) the derivative of the modulation function presents high values for certain angles θ. For illustrative purposes, Fig. 3 shows the behavior of $h(\theta)$ for $N = 10$ and $N = 50$; the plots were calculated using the number of addressable pixels in the experiment. In practice, the number of pixels limits the maximum available value for N: note that $h(\theta)$ for $N = 50$ is not well sampled. For high values of N, the subsampled modulation function does not properly represent $h(\theta)$ and thus, the uniformity and the length of the produced needle cannot be guaranteed. The inset shows the 2D profile of $h(\theta)$ ($N = 10$) on the sphere of reference. Since phase-mostly displays are not able to modulate real-valued distributions, function $h(\theta)$ is encoded using a cell-based hologram technique [28]. A description of how this method is used in beam design and the information regarding the calibration curves of the SLM can be found in [21,29,30].

OSA CONTINUUM

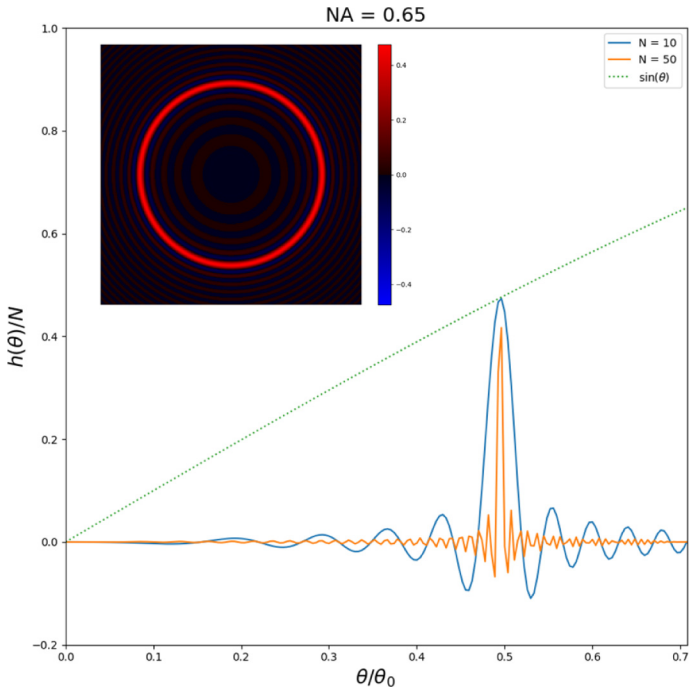

Fig. 3. Modulation function $h(\theta)$ for $N = 10$ and $N = 50$. The inset shows the 2D-profile of the modulation function $h(\theta)$ for $N = 10$.

3. Modeling experimental issues in optical needles

According to theoretical considerations, it was expected that the needles produced with modulation function $h(\theta)$ have to display an almost constant irradiance [22]. As described in the previous section, this fact is not strictly true. We have experimentally produced HON with $N = 4$, 6 and 10, using the optical setup depicted in Fig. 2. The corresponding distributions $h(\theta)$ were displayed on the SLM.

In order to generate a fair representation of the needle, the actuator shifts the position of the observation plane, so that the transverse irradiance at a certain distance z is recorded on CCD2 (z ranges from -50λ to 50λ). More than 900 images for each needle were recorded. Then, the elements of the transverse irradiance set were angularly averaged and arranged as a 2D distribution. The three produced needles ($N = 4$, 6 and 10) are shown on the left column of Fig. 4. Interestingly, the intensity of the needles on the axis z is not constant. A similar performance has been reported in several papers [10,22].

In our opinion, this behavior has been not systematically studied. It would be required to provide a better understanding on the reasons that might compromise the expected structure of the needle. The goal of the present paper is to provide an explanation to the behavior of HON generated with bulky optical elements. Accordingly, we developed a numerical simulation involving different variables.

The origin of the discrepancies might be related with the optical components used in the experimental setup: (i) the surfaces of the polarizers, wave plates or the SLM are not perfectly flat; (ii) a small fraction of light is not properly polarized after passing through a linear polarizer; the same happens with the SLMs, since some light is not well modulated when it crosses the displays; (iii) bulky optical components such as relay lenses or even the microscope objective

OSA CONTINUUM

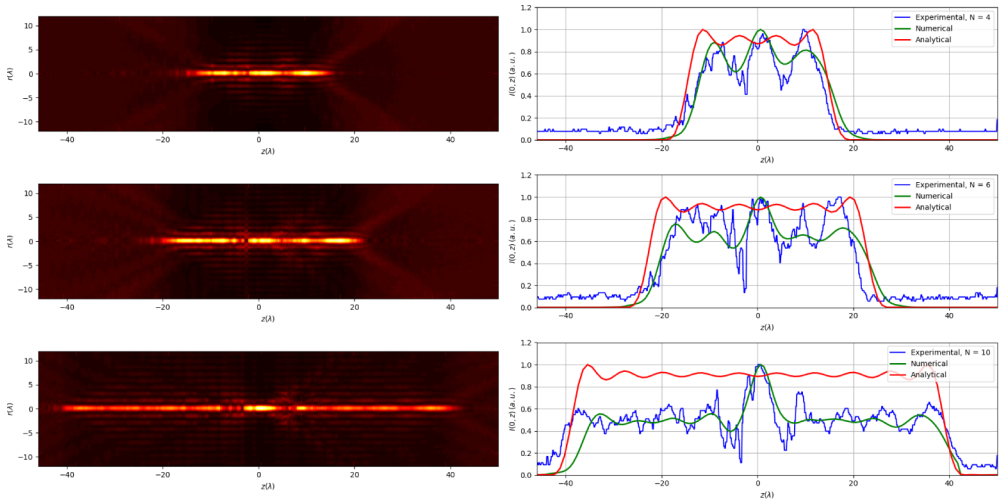

Fig. 4. Experimental results. Left column: HON for N =4, 6 and 10. Right column: Irradiance of the HON on the optical axis. Blue, green and red curves display experimental, estimated and theoretical data

might introduce a certain amount of spherical aberration. Finally, (iv) codification errors in the hologram connected with calibration errors and noise, might play a role in this problem.

The plots on the right side of Fig. 4 show the irradiance on the optical axis $I(0, z)$. The blue plot exhibits the raw values read from the corresponding image of the HON. The red curves were calculated using Eqs. (3 - 5). It is apparent that the analytical plots provides a fair explanation of the behavior of the experimental irradiance $I(0, z)$. In particular, measured and expected lengths are in good agreement in the three cases considered. Nevertheless, despite the theoretical needle profile is almost constant, several noticeable maxima and minima are present in the experimental measure.

According to the equations, the number of expected maxima is equal to parameter N, but in the measured distribution, the number of oscillations do not match number N [21]. Moreover, these fluctuations are more perceptible and the height of both maxima and minima varies depending on z. Notice that the number of detected maxima for the HON with N = 4, 6, and 10 is 3, 5 and 9 respectively. Another diverging behavior is detected in the HON with N = 10: in the case, the needle displays a more intense central maximum when compared with the other cases.

In order to provide an explanation on how the needle is distorted by the present optical setup, we numerically modeled the experimental behavior of the HON by taking into account the following variables:

1. As explained above (see last paragraph of section 2), the modulation function $h(\theta)$ is holographically encoded using the cell oriented technique [28]. Since the modulation curves show measurement errors, we model this effect by adding white noise in both amplitude and phase to $h(\theta)$ (note this function is real-valued with positive and negative values). According to the results reported in the Fig. 7 in Ref. [21], we estimated that the error in the amplitude is 2% of the maximum value; phase error ranges in $\pm 10^{\circ}$.

2. Despite optical surfaces are not perfectly uniform, they can be described as smooth distributions and thus, this fact changes the phase of the wavefront. We model this distortion by means of a Perlin noise generator [31]. The use of Perlin noise is appropriate in the context of this paper since it produces gradient controlled textures. In the present

OSA CONTINUUM

experiment we use $\lambda/10$ components. Accordingly, we introduce a wave aberration, using a Perlin generated surface with a phase peak-to-valley equivalent to $\pm 18°$.

3. A small amount of light passing through the polarizers is not properly polarized. Also, some light is not modulated by the SLM. We experimentally estimated that around 2% of the total light might be considered as background light.

4. The overall effect of the bulky optical elements of the system (lenses) produces spherical aberration. In order to prove this statement, we experimentally generated the 3D point spread function (see Fig. 5) in the same conditions that the needles depicted in Fig. 4; in this case, nothing was displayed on the SLM. This light distribution is compatible with a severe amount of spherical aberration A_s. We found that a suitable value is $A_s = 10\lambda$.

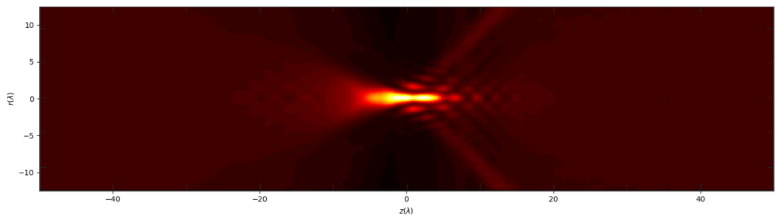

Fig. 5. Point spread function across the $z-$ axis

The green plots in Fig. 4, show the results for the three needles considered using the same simulation parameters. Now, the number of needle maxima is always correct and the calculated axial irradiance is closer to the experimental measure. In particular, when $N = 10$, the numerical estimation of the axial profile is very close to $I(0, z)$. Note that the needle central maximum is determined with more precision than in the theoretical case.

The simulation parameters modify the needle as follows: (i) the background light is responsible of the presence of a central peak. Note that for the three cases considered, the theoretical curve predicts a minimum at $z = 0$. The effect of the background light is particularly severe for $N = 10$. (ii) The combined effect of the spherical aberration and the lack of flatness change the number of maxima and the height of the minima. (iii) Holographic codification and modulation errors reduce the slope at the extremes of the needle.

It is noteworthy that the spherical aberration shifts the position of the needle. Indeed, the simulation provides this information. However, during the experimental recording of the needle, the actuator does not provide absolute positions. For this reason $z = 0$ is considered to be the center of the needle. Despite the numerical model simulates the needle in a more realistic way, the experimental axial distribution looks noisy. The origin of this distortion may be found in the mechanical drift of the piezoelectric actuator. We have not included this last step in the calculation because it is not related with the needle itself but with the recording process.

3.1. Comments on the code of the simulation

Code 1 [23], the script used for producing the results shown in Fig. 4, was written in MATLAB (The Mathworks, Inc., Natick, Massachusetts (US)) and comprises several functions and support files. This program can also also run under GNU Octave [32]. The code can be downloaded from [23].

The main script is found in `NEEDLES_MAIN.m`. The first lines of this file should be edited by the user in order to match the required experimental conditions. In particular, the user can define the values of variables such as the NA, parameter N, the spherical aberration or the expected flatness of the optical devices. Resolution parameters might be modified as well. The program

OSA CONTINUUM

calculates the intensity distribution at several planes normal to the direction of propagation using the Richards-Wolf formula [Eq. (3)].

The program ends up displaying several results: a 2D image of the xz plane of the the calculated HON, distribution $I(0,z)$ (intensity profile at the propagation axis), $I(r,z)$ (angular average irradiance of the needle as a function of z) and the irradiance of the beam at three selected transverse planes.

The main program uses several functions developed to perform specific tasks:

1. `abs2.m` computes the modulus square of a complex matrix of any size.
2. `colorMap.m` handles some custom color-maps.
3. `getAzimuRadialComps.m` returns the azimuthal (f_1) and radial (f_2) components of the vector angular spectrum $\mathbf{E}_0$ for a certain input beam $\mathbf{E}_S$.
4. `getFocusedField.m` calculates the Richard-Wolf integral using Fourier transforms.
5. `getHolograms.m` calculates the complex values to be displayed on the SLM acording to Arrizon's codification method [28]. This function requires the calibration information of the display available at `AmplitudeValues_SLM1.txt` and `AmplitudeValues_SLM2.txt`. These files provide specific information for the displays used (Holoeye HEO 0017). The function produce the holograms for two orthogonal directions of polarization [29]. Since the needles produced in this paper are linearly polarized only one SLM is required to encode modulation function $h(\theta)$.
6. `getPerlinNoiseImage.m` generates Perlin noise 2D distributions for simulating the lack of flatness of the optical components.
7. `getRefSphereCoords.m` returns the azimuthal and polar coordinates at the entrance pupil of the microscope lens.
8. `hologramSimulator.m`: Simulates the behavior of the SLM, according to its complex modulation capabilities and filters the high order holographic terms. This function takes into account the uncertainty induced in the calibration process.
9. `shiftedFFT.m` (`ishiftedFFT.m`) calculates a properly shifted, forward (backward) Fourier transform.
10. `normalize2D.m` normalizes arrays in the range [0,1].

4. Conclusion

Highly focused needles produced with holographic devices present distortions and a non-uniform structure as a consequence of the use of bulky optical components. We analyzed how display modulation errors, holographic codification, lack of flatness of the optical components, light that is not properly polarized when passes through a polarizer and spherical aberration degrade the quality of the needle. These issues were modeled by means of a numerical simulation and we found that not all of them affect the needle in the same way: a central peak can be present as a consequence of background light, and spherical aberration and surface distortions modify the on-axis number of maxima and the height of the minima. Less important is the effect of modulation errors and holographic codification because they just slightly modify the slope at the beginning and at the end of the needle. In summary, the numerical analysis of the distortions introduced by the optical components provides a better understanding on how the quality of a HON is compromised. We found a good agreement between experimental results and the numerically estimated needles.

OSA CONTINUUM

Funding

Ministerio de Economía y Competitividad (MINECO) (FIS2016-75147-C3-1-P).

References

1. J. H. McLeod, "The axicon: a new type of optical element," J. Opt. Soc. Am. **44**(8), 592–597 (1954).
2. D. McGloin and K. Dholakia, "Bessel beams: diffraction in a new light," Contemp. Phys. **46**(1), 15–28 (2005).
3. H. Wang, L. Shi, B. Lukyanchuk, C. Sheppard, and C. T. Chong, "Creation of a needle of longitudinally polarized light in vacuum using binary optics," Nat. Photonics **2**(8), 501–505 (2008).
4. K. Rajesh, Z. Jaroszewicz, and P. Anbarasan, "Improvement of lens axicon's performance for longitudinally polarized beam generation by adding a dedicated phase transmittance," Opt. Express **18**(26), 26799–26805 (2010).
5. K. Kitamura, K. Sakai, and S. Noda, "Sub-wavelength focal spot with long depth of focus generated by radially polarized, narrow-width annular beam," Opt. Express **18**(5), 4518–4525 (2010).
6. J. Lin, K. Yin, Y. Li, and J. Tan, "Achievement of longitudinally polarized focusing with long focal depth by amplitude modulation," Opt. Lett. **36**(7), 1185–1187 (2011).
7. H. Dehez, A. April, and M. Piché, "Needles of longitudinally polarized light: guidelines for minimum spot size and tunable axial extent," Opt. Express **20**(14), 14891–14905 (2012).
8. C. J. Sheppard and S. Mehta, "Three-level filter for increased depth of focus and bessel beam generation," Opt. Express **20**(25), 27212–27221 (2012).
9. Y. Zha, J. Wei, H. Wang, and F. Gan, "Creation of an ultra-long depth of focus super-resolution longitudinally polarized beam with a ternary optical element," J. Opt. **15**(7), 075703 (2013).
10. G. Yuan, E. T. Rogers, T. Roy, G. Adamo, Z. Shen, and N. I. Zheludev, "Planar super-oscillatory lens for sub-diffraction optical needles at violet wavelengths," Sci. Rep. **4**(1), 6333 (2014).
11. C. Sheppard, "Optimization of pupil filters for maximal signal concentration factor," Opt. Lett. **40**(4), 550–553 (2015).
12. F. Qin, K. Huang, J. Wu, J. Jiao, X. Luo, C. Qiu, and M. Hong, "Shaping a subwavelength needle with ultra-long focal length by focusing azimuthally polarized light," Sci. Rep. **5**(1), 9977 (2015).
13. J. Xing, J. Kim, and H. Yoo, "Design and fabrication of an optical probe with a phase filter for extended depth of focus," Opt. Express **24**(2), 1037–1044 (2016).
14. M. Veysi, C. Guclu, O. Boyraz, and F. Capolino, "Reflective metasurface lens with an elongated needle-shaped focus," J. Opt. Soc. Am. B **34**(2), 374–382 (2017).
15. Y. Yu, H. Huang, M. Zhou, and Q. Zhan, "Creation of a multi-segmented optical needle with prescribed length and spacing using the radiation pattern from a sectional-uniform line source," Sci. Rep. **7**(1), 10708 (2017).
16. L. Turquet, X. Zang, J.-P. Kakko, H. Lipsanen, G. Bautista, and M. Kauranen, "Demonstration of longitudinally polarized optical needles," Opt. Express **26**(21), 27572–27584 (2018).
17. R. Dharmavarapu, S. Bhattacharya, and S. Juodkazis, "Diffractive optics for axial intensity shaping of Bessel beams," J. Opt. **20**(8), 085606 (2018).
18. E. T. Rogers, J. Lindberg, T. Roy, S. Savo, J. E. Chad, M. R. Dennis, and N. I. Zheludev, "A super-oscillatory lens optical microscope for subwavelength imaging," Nat. Mater. **11**(5), 432–435 (2012).
19. Z. Gan, Y. Cao, R. A. Evans, and M. Gu, "Three-dimensional deep sub-diffraction optical beam lithography with 9 nm feature size," Nat. Commun. **4**(1), 2061 (2013).
20. S. Payeur, S. Fourmaux, B. Schmidt, J. MacLean, C. Tchervenkov, F. Légaré, M. Piché, and J. Kieffer, "Generation of a beam of fast electrons by tightly focusing a radially polarized ultrashort laser pulse," Appl. Phys. Lett. **101**(4), 041105 (2012).
21. R. Martínez-Herrero, D. Maluenda, I. Juvells, and A. Carnicer, "Synthesis of light needles with tunable length and nearly constant irradiance," Sci. Rep. **8**(1), 2657 (2018).
22. Y. Kozawa and S. Sato, "Long depth-of-focus imaging by a non-diffracting optical needle under strong aberration," in *Lasers and Electro-Optics (CLEO), 2017 Conference on*, (IEEE, 2017) pp. 1–2.
23. D. Maluenda, I. Juvells, R. Martínez-Herrero, and A. Carnicer, "A numerical tool to evaluate highly focused holographic optical needles," figshare (2019), https://figshare.com/s/d91bac6b21e43939cbcb.
24. B. Richards and E. Wolf, "Electromagnetic diffraction in optical systems. II. structure of the image field in an aplanatic system," Proc. R. Soc. A **253**(1274), 358–379 (1959).
25. T. Grosjean and D. Courjon, "Polarization filtering induced by imaging systems: effect on image structure," Phys. Rev. E **67**(4), 046611 (2003).
26. L. Novotny and B. Hecht, *Principles of nano-optics* (Cambridge University Press, 2012).
27. T. Čižmár and K. Dholakia, "Tunable Bessel light modes: engineering the axial propagation," Opt. Express **17**(18), 15558–15570 (2009).
28. V. Arrizón, L. A. González, R. Ponce, and A. Serrano-Heredia, "Computer-generated holograms with optimum bandwidths obtained with twisted-nematic liquid-crystal displays," Appl. Opt. **44**(9), 1625–1634 (2005).
29. D. Maluenda, I. Juvells, R. Martínez-Herrero, and A. Carnicer, "Reconfigurable beams with arbitrary polarization and shape distributions at a given plane," Opt. Express **21**(5), 5432–5439 (2013).
30. D. Maluenda, A. Carnicer, R. Martínez-Herrero, I. Juvells, and B. Javidi, "Optical encryption using photon-counting polarimetric imaging," Opt. Express **23**(2), 655–666 (2015).

OSA CONTINUUM

31. K. Perlin, "An image synthesizer," ACM Siggraph Comput. Graph. **19**(3), 287–296 (1985).
32. J. W. Eaton, D. Bateman, S. Hauberg, and R. Wehbring, *GNU Octave version 4.2.1 manual: a high-level interactive language for numerical computations* (2017).